

VISUALIZING NUCLEOSOME PHASE SEPARATION WITH SUPER RESOLUTION
MICROSCOPY

PHD PRELIMINARY EXAMINATION

DEPARTMENT OF PHYSICS

BY
CLAYTON W. SEITZ

FALL 2023

TABLE OF CONTENTS

ABSTRACT	iii
1 Introduction	1
1.1 Single molecule localization microscopy	1
1.2 The definition of resolution in SMLM	1
1.3 Towards time-resolved SMLM	2
1.4 Enhanced SMLM with photon statistics	4
1.5 Super-resolution of transcriptional condensates in living cells	6
2 Results	8
2.1 Deep networks outperform MLE in dense localization	8
2.2 Counting quantum dots with a Hidden Markov Model	9
2.3 Super-resolution of nucleosome-BRD4 interactions in living cells	9
3 Discussion and Future Aims	10
3.1 Specific Aim 1: Integrate deep models with counting algorithms for enhanced SMLM	10
3.2 Specific Aim 2: Determine a role of chromatin architecture in phase separation	11
4 Materials and Methods	12
4.1 Super-resolution imaging of nucleosome nanodomains	12
4.2 Localization of isolated emitters with maximum likelihood estimation	13
4.3 The Cramer-Rao lower bound	15
4.4 Dense localization with convolutional neural networks	16
4.5 Hidden Markov Model for counting fluorescent emitters	16
4.6 Computation of Besag's L-function	18
4.7 Fourier Ring Correlation	19
5 Supplemental Information	20
5.1 Noise model for CMOS cameras used for MLE	20
5.2 Integrated isotropic Gaussian point spread functions	21
6 References	22

ABSTRACT

Single-molecule localization microscopy (SMLM) techniques, such as direct stochastic optical reconstruction microscopy (dSTORM), can be used to produce a pointillist representation of fluorescently-labeled biological structures at diffraction-unlimited precision. Direct STORM approaches leverage the deactivation of standard fluorescent tags, followed by spontaneous or photoinduced reactivation, allowing resolution of fluorophores at distances below the diffraction limit. This basic principle remains one of the method's primary limitations - standard SMLM fitting routines require tight control of activation and reactivation to maintain sparse emitters, presenting a tradeoff between imaging speed and labeling density. Here, I present two parallel projects, which aim to push the current state of the art in SMLM and apply SMLM to the study of gene regulation, respectively. The former represents a novel localization technique for dense SMLM based on deep probabilistic modeling and photon statistics. In the latter, conventional dSTORM is adapted for live cell imaging of chromatin nanodomains, demonstrating that BRD4 protein concentrates in nucleosome depleted regions.

1 Introduction

1.1 *Single molecule localization microscopy*

Single molecule localization microscopy (SMLM) relies on the temporal resolution of fluorophores in the sample whose spatially overlapping point spread functions would otherwise render them unresolvable at the detector. SMLM techniques, such as stochastic optical reconstruction microscopy (STORM) and photo-activated localization microscopy (PALM) remain desirable for super-resolution imaging of many cellular structures, due to their cost-effective implementation and diffraction unlimited resolution (Schermerle 2019). Common strategies for the temporal separation of molecules involve transient intramolecular rearrangements to switch from dark to fluorescent states or the exploitation of non-emitting molecular radicals. For direct STORM, rhodamine derivatives can undergo intersystem crossing to a triplet state, which can be reduced by thiols to form a dark radical species. The dark state can then be quenched by oxidative processes, driving the fluorophore back to its ground state (Figure 1a). Long dark state lifetimes are commonly used in STORM imaging in order to maintain sparse activation and high resolution.

1.2 *The definition of resolution in SMLM*

The distribution of a particular biomolecule in the cell can be described as a probability density over a two-dimensional space, casting super-resolution essentially a density estimation problem. Intuitively, the spatial resolution of SMLM images then increases as we draw more samples from this density - a concept which is made mathematically precise by the so-called Fourier ring correlation or FRC. Using FRC, one can compute image resolution as the spatial frequency at which a correlation function in the frequency domain drops below a threshold, typically taken to be $1/7$ (Figure 2). According to this theory, reducing localization uncertainty while increasing the number of samples, results in an increase in image

resolution (Nieuwenhuizen 2013). However, there of course remains a fundamental limit to the the minimal localization uncertainty which can be obtained.

Localization uncertainty, typically the RMSE of a maximum likelihood or similar statistical estimator, is bounded from below by the inverse of the Fisher information matrix, known as the Cramer-Rao lower bound (Chao 2016). Localization uncertainties in sparse conditions are often tens of nanometers, although recent work on integration of Bayesian priors with modulation enhanced SMLM (meSMLM) or structured illumination with MIN-FLUX, has reduced spatial resolution below 1 nanometer (Kalisvaart 2022, Gwosh 2020). Nevertheless, managing the increase in localization uncertainty at high labeling density still remains a major bottleneck to SMLM. Static uncertainty due to molecular crowding can be partially ameliorated by using pairwise or higher-order temporal correlations within a pixel neighborhood, known as stochastic optical fluctuation imaging or SOFI (Dertinger 2009). Other approaches such as stimulated emission and depletion (STED) imaging bring control over the photophysical state of a chosen subset of the sample, yet the need for laser scanning prevents widespread application in live-cell studies. The spatial resolution and relative simplicity of SMLM techniques remains unmatched, inciting an effort to increase the resolution of SMLM techniques and explore avenues towards time resolved SMLM.

1.3 Towards time-resolved SMLM

Previous approaches to improving the resolution of SMLM by increasing number of localizations per unit time have been primarily based on a combination of intensity measurements and probabilistic deep learning. Standard postprocessing for STORM imaging includes maximum likelihood estimation of molecular coordinates using Gaussian point spread function models. However, in dense STORM, the parameter space volume grows exponentially with the number of emitters, which is often unknown apriori. Exploration of this high dimensional parameter space in dense STORM is often intractable.

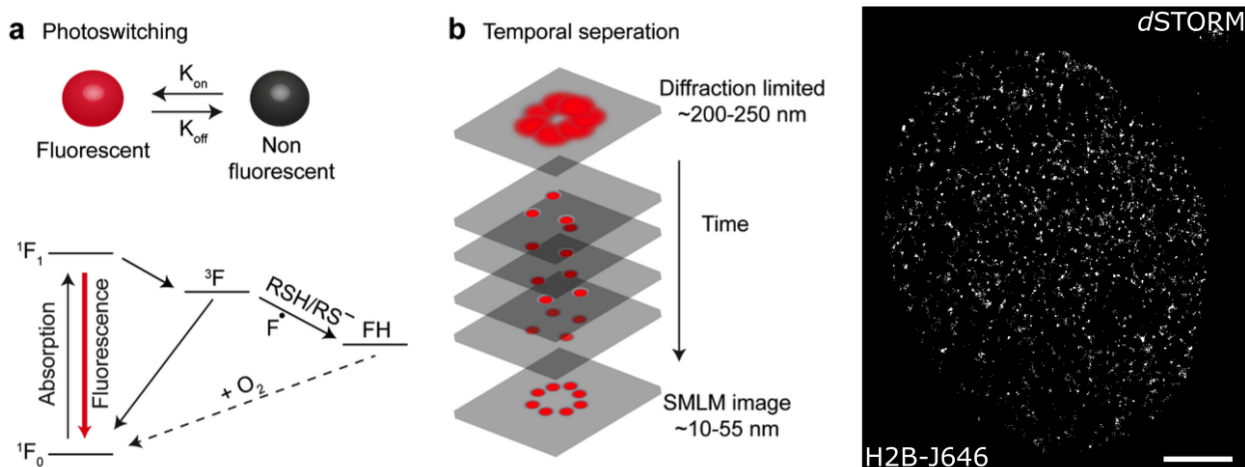


Figure 1: Stochastic optical reconstruction microscopy (STORM). (A) Single molecules are resolved by separating their fluorescent emission in time, using fluorophores with multiple photophysical states (B) Example super-resolution image of H2B protein in a living HeLa cell nucleus at 37C

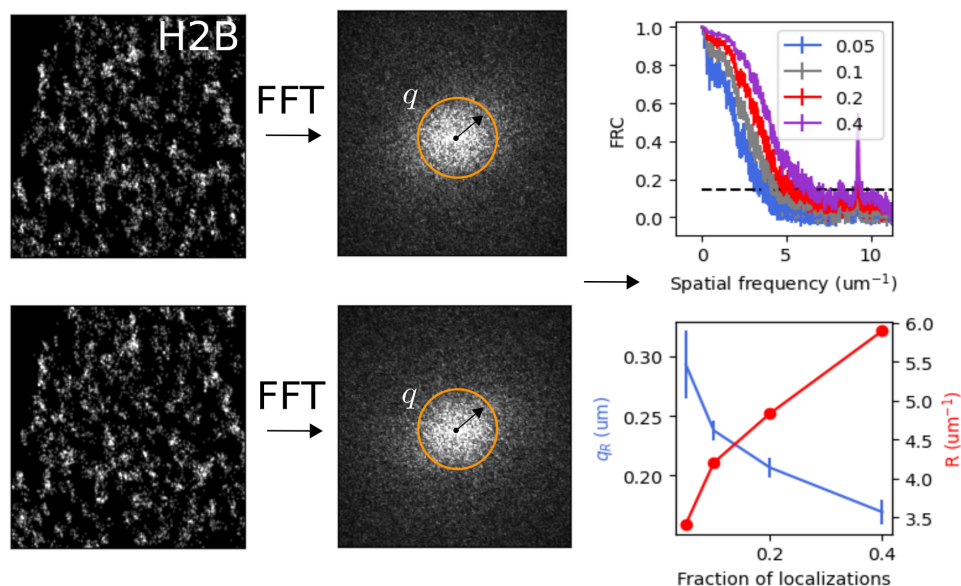


Figure 2: Dense localization increases image resolution and enables time-resolved STORM. A pair of subsets is drawn from the full list of localizations for various fractions of the total number of localizations, and isotropic Gaussian kernel density estimation is performed with $\sigma = 20\text{nm}$. The Fourier Ring Correlation (Methods) is calculated for the pair and plotted as a function of spatial frequency.

In one approach to this issue, deep generative models have been used to learn the generating distribution of images of cellular structures from super-resolution data. Trained models can then be used to predict super-resolution images based on sparse localizations or widefield images (Ouyang 2018; Barth 2020; Chen 2023). Other approaches leverage convolutional neural networks (CNNs) to transform dense images into a localization map (Nehme 2020; Speiser 2021). In general, convolutional neural networks are well-known for their ability to discover higher order spatial structure in an image to infer latent variables. This can be seen as learning a translation from SMLM image intensities to pixel-wise probabilities of emitter occupancy.

While the use of deep models has shown great promise for dense SMLM, there remains two major drawbacks. First, CNNs are often unconstrained by physical variables, such as the total number of fluorescent emitters in a given region of interest. Second, CNNs do not explicitly model the image likelihood, making computation of localization uncertainties challenging. Therefore, we introduce a novel inference scheme which (i) infers the number fluorescent emitters in the ROI by modeling photon statistics measured with a photon counting camera (ii) permits relatively fast computation of localization uncertainty using a gradient-based Markov Chain Monte Carlo (MCMC) scheme, known as Langevin dynamics.

1.4 Enhanced SMLM with photon statistics

Molecular counting with photon statistics has a fairly simple motivation: a photon emitted by a fluorescent molecule can only be detected once. Coincidence of photons at multiple detector elements provides evidence that two or more molecules are present in the imaged region. Combining the ideas of conventional super-resolution approaches, such as dSTORM, with photon statistics may prove to be a powerful set of methods for bioimaging. Innovations in single photon detection technologies have begun to be integrated into fluorescence microscopes (Forbes 2019). Importantly, single photon detectors such as single photon avalanche

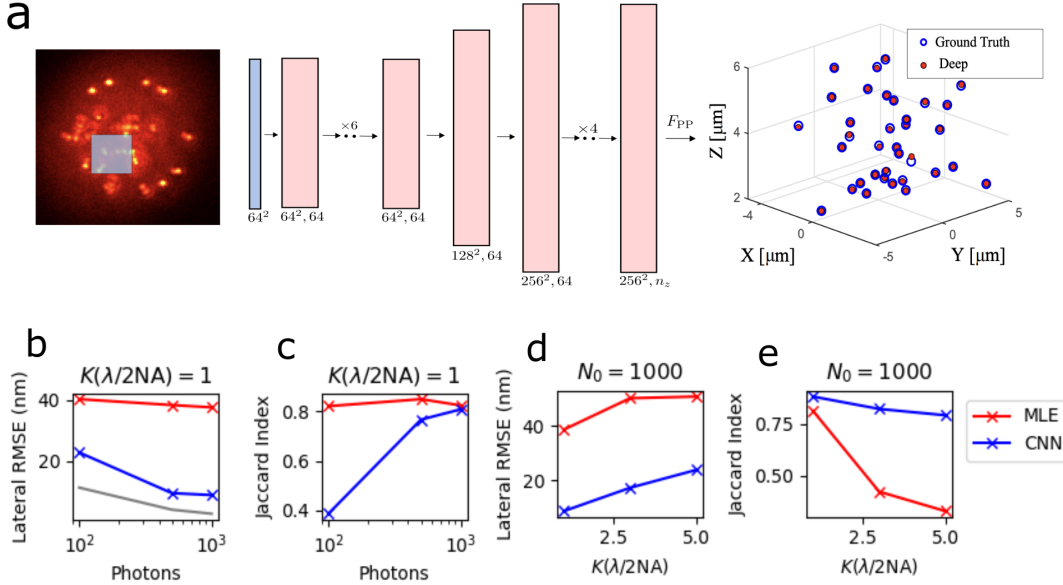


Figure 3: Deep networks outperform MLE in dense localization

(A) DeepSTORM3D architecture with 612K trainable parameters used for localization. (B-E) Lateral root mean squared error and Jaccard index of MLE and CNN estimators with respect to the incident photon count and the number of molecules within the diffraction limit $\lambda/2NA$. Cramer-Rao lower bound shown in gray

photodiodes (SPAD) arrays have three orders of magnitude higher temporal resolutions than standard sCMOS cameras, single photon sensitivity, and theoretically zero readout noise. Such properties make these devices highly desirable for imaging applications; however, application of SPAD arrays in imaging have been limited to small bundles of detector elements combined with laser scanning (Israel 2017; Forbes 2019; Tenne 2019). Recently, SPAD cameras have become commercially available, potentially bringing many of the advantages of single photon detection to widefield fluorescence microscopy. As a proof of principle, we image quantum dots (QDs) at 1 MHz with a 512x512 SPAD array, and devise a fully probabilistic model that blends a Hidden Markov Model (HMM), CNN, and MCMC for dense localization microscopy (See Methods).

1.5 *Super-resolution of transcriptional condensates in living cells*

Super-resolution imaging with intensity information alone remains a highly valuable technique, and we demonstrate this by live cell super-resolution imaging of nucleosome-BRD4 interactions in transcriptional condensates. The nucleosome is an octamer of histone proteins and is the fundamental unit of chromatin - a complex of DNA and protein which forms the basic scaffold for a variety of biomolecular processes in the nucleus. Super-resolved nucleosome organization has been studied extensively in various epigenomic states to reveal segregated nanoclusters, dispersed nanodomains, and compact large aggregates. Indeed, nucleosomes assemble into heterogeneous clusters of variable sizes, interspersed with nucleosome-depleted regions (Ricci 2015). Histones can be decorated with various post-translational modifications such as acetylation, methylation, phosphorylation, and ubiquitination. The recruitment of proteins and complexes with specific enzymatic activities is now a well-accepted dogma of how modifications mediate their function. Histone modifications can influence the transcription of genes, and many other DNA processes such as repair, replication and recombination (Bannister and Kouzarides, 2011).

Here, we use a direct STORM approach to study spatial organization of nucleosomes in living cells, with a particular focus on the structure of phase separated condensates containing bromodomain protein 4 (BRD4) protein. BRD4 plays an important role in diverse cellular functions such as transcription, replication, epigenetic regulation, and DNA repair, and has been implicated in cancer and autoimmune diseases. BRD4 acetylates Lysine 122 on H3 (H3K122), a residue critical for nucleosome stability, resulting in nucleosome eviction and chromatin decompaction (Devaiah 2016). The intrinsically disordered regions (IDRs) of BRD4 are thought to facilitate its phase separation with coactivators such as MED1. The phase separation properties of BRD4 have been well-studied in several cell lines (Han 2020), and in the context of super-enhancers (Sabari 2018).

Selective bromodomain inhibitors, such as JQ1 are often employed to displace BRD4 pro-

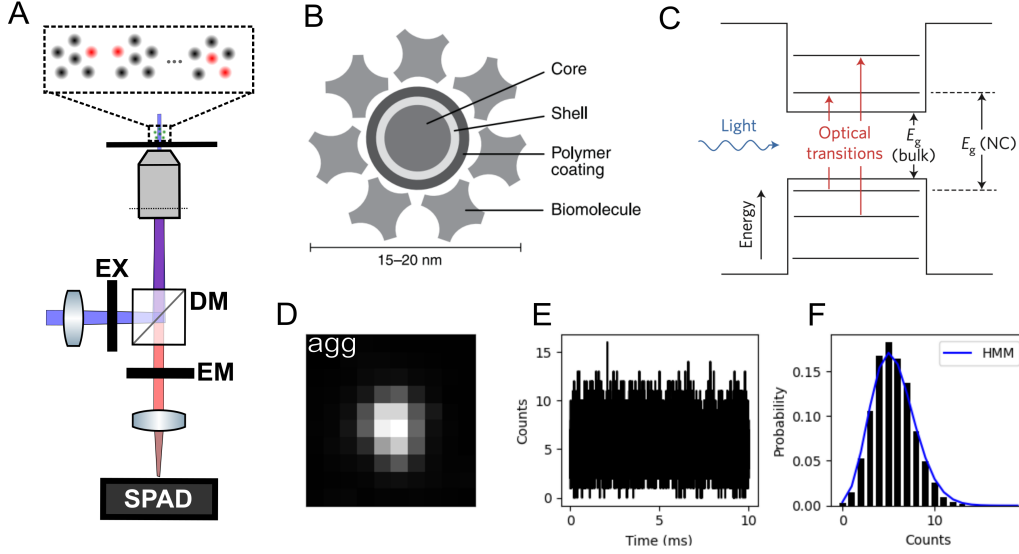


Figure 4: Counting quantum dots with a Hidden Markov Model. (A) Cartoon representing photon counting of an aggregate of quantum dots (B,C) Structure of a single CdSe/ZnS quantum dot and its optical transitions (D) Summed image of a QD aggregate. (E) photon counts over time for the sum in (D) (F) Histogram of counts over time and HMM fit

tein from chromatin (Filippakopoulos 2010). 1,6-hexanediol (1,6-HD), an aliphatic alcohol, can inhibit weak hydrophobic protein-protein interactions required for the droplet formation (droplet melting activity) and is widely used to elucidate the formation of nuclear bodies (Duster 2021). However, the relationship of BRD4, and phase separation at large, with the spatial structure of nucleosome nanodomains remains unclear. As BRD4 is a critical component of phase separated transcriptional condensates, we take a complementary approach, consisting of specific and non-specific inhibition of BRD4-containing condensates using small molecule drugs and BRD4 mutation or knockdown.

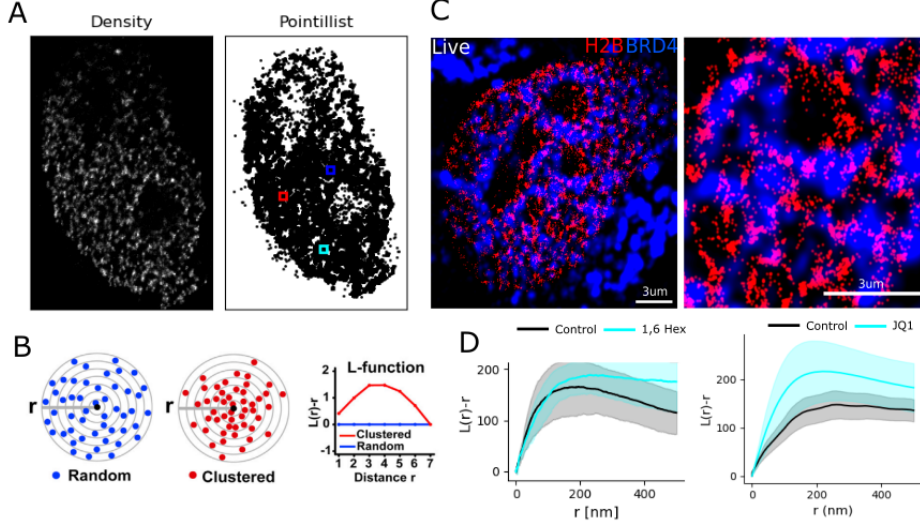


Figure 5: Super resolution of chromatin structure at BRD4-positive loci. (A) Density and pointillist representation of nucleosome organization in a living cell recovered with MLE (B) Principle of Besag’s L-Function for cluster analysis (C) Average L-function for living Hela cells exposed to 5 percent 1,6 Hexanediol or 1uM JQ1 for 8h. Envelope drawn at one standard deviation

2 Results

2.1 Deep networks outperform MLE in dense localization

Two major factors contribute to localization errors in SMLM: (i) the noise characteristics of CMOS cameras and (ii) crowding of molecules within a diffraction limited region. Maximum likelihood estimation (MLE) is frequently used for isolated molecules and high signal levels, retaining localization errors 40nm (Figure 3b). However, MLE performance tends to degrade in low SNR and dense regimes where the number of emitters within the diffraction limit is greater than one ($K(\lambda/2NA) > 1$). We employ a convolutional neural network called DeepSTORM, which successively upsamples a monochrome image and outputs a localization map, which can be post-processed to produce molecular coordinates in 2D or 3D (Figure 3a). We demonstrate that this architecture can outperform maximum likelihood estimation

for all signal levels and molecular densities tested (Figure 3b-e).

2.2 *Counting quantum dots with a Hidden Markov Model*

Dense aggregates of proteins and nucleic acids with molecular spacing below the diffraction limit are commonplace in the nucleus, creating the need for accurate counting techniques. The ability to accurately count fluorescent emitters using photon statistics has been so far limited to confocal microscopy setups, which are not typically used when imaging dynamics in living cells. As a proof of principle, we imaged organic quantum dots 15-20nm in size. These nanocrystals are composed of a CdSe semiconductor core, ZnS semiconductor shell, and an amphiphilic polymer coating is applied to confer water solubility and additional functionalization with antibodies, oligonucleotides, etc (Figure 4B). We imaged quantum dots coated on a glass coverslip with a SPAD camera at 1 MHz, and applied our HMM to photon counts from both isolated emitters as well as dense aggregates (Figure 4A,D). Our data indicates that a Poisson HMM models the data well, as measured by the log-likelihood of the sequence of photon counts and distribution of emissions over time (Figure 4E,F). Model selection is carried out purely based on log-likelihood of the sequence.

2.3 *Super-resolution of nucleosome-BRD4 interactions in living cells*

Here, we use the HaloTag system, a modified haloalkane dehalogenase designed to covalently bind to synthetic ligands (Los 2008). The HaloTag protein is fused to H2B and is then bound by a rhodamine-derived fluorescent ligands, JF549 or JF646 (Grimm 2015). Two-color imaging of H2B-JF646 and BRD4-GFP showed that BRD4-GFP is present in nucleosome depleted regions, and that BRD4-GFP makes direct contact with the chromatin scaffold (Figure 5C). Exposure of cells to 1,6 Hexanediol promoted an increase in nucleosome cluster sizes, while JQ1 exposure significantly condensed nucleosome clusters (Figure 5D).

3 Discussion and Future Aims

3.1 *Specific Aim 1: Integrate deep models with counting algorithms for enhanced SMLM*

Rationale and hypothesis

We have demonstrated that deep learning algorithms can outperform standard maximum likelihood estimators in low SNR and high density regimes, indicating this is a suitable first step in our SMLM pipeline. In addition, our HMM appears to accurately model the photon detection process. The application of Bayesian methods to prevent overfitting with HMMs is common, and Hierarchical Dirichlet Prior HMM or HDP-HMM may be an appropriate choice in future work.

The HMM proves useful because we can actually observe the fluorescence in time, meaning that we have many samples from a Poisson distribution on photon counts. If we just take the sum, we have a single sample from another Poisson distribution (which would have a larger rate parameter), which is insufficient for predicting the underlying mass function, and therefore fitting the number of emitters. We could obtain this with many frames, but this is wasteful, and would take potentially seconds, when we can estimate it in much shorter periods of time

Computational Approach

Exploration of the high dimensional parameter space in dense STORM is fundamentally intractable. Therefore, the DeepSTORM architecture will be adopted to a probabilistic setting by modifying the output by adding a softmax layer. The arbitrary threshold for Bernoulli probabilities at each pixel conventionally used in DeepSTORM will be removed, and the maximum a posteriori (MAP) number of localizations will be selected from the

probability map. We will then attempt to implement a gradient-based Markov Chain Monte Carlo (MCMC) routine, for computing localization uncertainties.

3.2 Specific Aim 2: Determine a role of chromatin architecture in phase separation

Rationale and hypothesis

We have demonstrated by two-color live cell super resolution imaging of H2B and BRD4-GFP that BRD4-GFP protein is present in nucleosome depleted regions (NDRs) in the nucleus. The increase in cluster sizes upon exposure to 1,6 Hexanediol suggests that nucleosome nanodomains may merge after non-specific inhibition of phase separation, while the average spacing of nucleosomes remains. The significant condensation after exposure to JQ1 suggests that BRD4 may be involved in the maintenance of the degree of chromatin condensation, but does not affect the average sizes of nucleosome clusters. Although BRD4-GFP is clearly present in NDRs, there is a significant overlap of H2B and BRD4 signals, leading us to conclude that BRD4 may permeate some nucleosome-dense regions as well. Ultimately, results of treatment of HeLa cells with non-specific and specific phase separation inhibitors suggest that further study into the mechanism of BRD4-specific inhibition. We believe that BRD4 silencing and mutation of BRD4 residues would provide valuable insights into the role of the chromatin scaffold in the formation of transcriptional condensates.

Previous efforts have demonstrated the acetylated histone reading function of BRD4 is proceeded by recruitment of additional cofactors and chromatin reorganization. Additional perturbations to BRD4 functions may provide a more complete picture of how BRD4-positive nuclear bodies interact with the chromatin scaffold. Our preliminary data suggests that transcriptional condensates in the nucleus may be stabilized by interactions with neighboring nucleosome clusters. Given that transcriptional condensates associate with accessible DNA,

we expect that their depletion by specific inhibition of BRD4 functions will lead to chromatin condensation. Moreover, we expect the action of specific antagonists against BRD4 or its expression will have a distinct effect compared to 1,6 Hexanediol, which may act on the chromatin scaffold directly (Itoh 2021).

Experimental Approach

The chromatin binding modules of BRD4 suggest that phase separated transcriptional condensates in the nucleus are, in part, dependent on nucleosome-BRD4 binding interactions. We propose live-cell super-resolution experiments to determine the nature of the interaction between BRD4 and the chromatin architecture in the formation of BRD4-condensates. To do this, we have first designed siRNAs to knockdown expression of BRD4 protein in HeLa cells, which will determine the effect of global BRD4 loss on chromatin architecture. We will then express wild type and BRD4 mutant plasmids which have mutated Bromodomains. Other experiments may involve mutating the intrinsically disordered regions (IDRs) of BRD4 to impair the phase separation abilities of BRD4. Finally, in order to address the possibility that small molecule drugs such as JQ1 impact structure of the chromatin scaffold, independent of BRD4, we will carry out additional live-cell super-resolution experiments combining BRD4 RNA silencing with JQ1 treatment.

4 Materials and Methods

4.1 Super-resolution imaging of nucleosome nanodomains

After transient transfection, H2B-HaloTag HeLa cells were incubated with JF646 HaloTag ligand overnight. Living HeLa cells were imaged in a dSTORM photoswitching buffer containing 100mM MEA, 50 ug/ml Glucose Oxidase, and 3.4 mg/ml Catalase (Sigma). Buffer pH was adjusted to 8 using HCl. Movies were collected using a customized Olympus IX83 micro-

scope equipped with an Olympus 60X 1.25NA oil-immersion objective. Fluorescence images were projected onto an ORCA-Fusion sCMOS camera (Hamamatsu). The microscope was controlled using Micromanager software. JF646 molecules were illuminated with a 640nm laser held at 20mW, as measured at the back focal plane of the objective. Frames were captured at 100fps. Sparse localizations were localized with maximum likelihood estimation.

4.2 Localization of isolated emitters with maximum likelihood estimation

For each pixel of a CMOS camera, the number of photoelectrons S_k is multiplied by a gain factor g_k [ADU/ e^-], which generally must be measured during calibration. The readout noise per pixel ξ_k is Gaussian with some pixel-specific offset o_k (Figure 2a) and variance σ_k^2 (Figure 2b). Ultimately, we have a Poisson component of the noise, which scales with the signal level and a Gaussian component, which does not. Therefore, in a single exposure, we measure:

$$\vec{H} = \vec{S} + \vec{\xi} \quad (1)$$

What we are after is the joint distribution $P(\vec{H})$. Fundamental probability theory states that the distribution of H_k is the convolution of the distributions of S_k and ξ_k ,

$$P(H_k|\theta) = P(S_k) \otimes P(\xi_k) \quad (2)$$

$$= A \sum_{q=0}^{\infty} \frac{1}{q!} e^{-\mu_k} \mu_k^q \frac{1}{\sqrt{2\pi\sigma_k^2}} e^{-\frac{(H_k - g_k q - o_k)^2}{2\sigma_k^2}} \quad (3)$$

where $P(\xi_k) = \mathcal{N}(o_k, \sigma_k^2)$ and $P(S_k) = \text{Poisson}(g_k \mu_k)$, A is some normalization constant and \otimes represents convolution. The rate μ_k is computed by the forward model which is an integration of the point spread function of the microscope (Supp. Eq 8). In practice, (3)

is difficult to work with, so we look for an approximation. We will use the Poisson-Normal approximation for simplification. Consider,

$$\xi_k - o_k + \sigma_k^2 \sim \mathcal{N}(\sigma_k^2, \sigma_k^2) \approx \text{Poisson}(\sigma_k^2)$$

Since $H_k = S_k + \xi_k$, we transform $H'_k = H_k - o_k + \sigma_k^2$, which is distributed according to

$$H'_k \sim \text{Poisson}(\mu'_k)$$

where $\mu'_k = g_k \mu_k + \sigma_k^2$. This result can be seen from the fact the the convolution of two Poisson distributions is also Poisson. The quality of this approximation will degrade with decreasing signal level, since the Poisson distribution does not retain its Gaussian shape at low expected counts. Nevertheless, the quality of the approximation appears to increase exponentially with the expected count, as measured by the Komogonov distance between the convolution distribution (4) and its Poisson approximation (Figure 8).

In this work, we suppose that molecules really do have an exact location in space over the integration interval. In pratice, this is only an approximation since molecules can diffuse at physiological temperatures, and our exposure time would need to tend to zero for this to be exactly true. If we suppose that we can collect a sufficient amount of photons in a short enough time, such that a definite position exists, the following optimization problem is defined

$$\theta_{\text{MLE}} = \underset{\theta}{\operatorname{argmax}} \prod_k P(H_k|\theta) = \underset{\theta}{\operatorname{argmin}} - \sum_k \log P(H_k|\theta)$$

where θ_{MLE} represents the maximum likelihood coordinates of a fluorescent molecule. Maximum likelihood estimation (MLE) is a natural choice, since optimization of coordinates under a Poisson likelihood is tractable. Under the Poisson approximation, the model negative log-likelihood is

$$\ell(\vec{H}|\theta) = -\log \prod_k \frac{e^{-(\mu'_k)} (\mu'_k)^{n_k}}{n_k!} \quad (4)$$

$$= \sum_k \log n_k! + \mu'_k - n_k \log (\mu'_k) \quad (5)$$

A stirling approximation can be made for the above log-factorial. First order derivatives of this sum can often be computed analytically, depending on μ .

To summarize, our localization method depends on a likelihood for independent Poisson variables, where the parameter of each Poisson variable is a function of other latent variables (molecular coordinates). It is an analytical likelihood, and we have shown that we can write it down in terms of error functions. However, the full distribution over images cannot be written down explicitly - it can only be written at a single point in parameter space. We compute the likelihood first using the forward model (Supp. Eq 8) and then compute the Poisson data likelihood using calculated rates. This intermediate step is what prevents us from being able to write down a likelihood only in terms of common distributions.

4.3 The Cramer-Rao lower bound

The Poisson approximation is also convenient for computing the Fisher information matrix for θ_{MLE} and thus the Cramer-Rao lower bound, which bounds the variance of a statistical estimator of θ_{MLE} , from below (Chao 2016). The Fisher information is

$$I_{ij}(\theta) = \mathbb{E} \left(\frac{\partial \ell}{\partial \theta_i} \frac{\partial \ell}{\partial \theta_j} \right) \quad (6)$$

Let $\mu'_k = \mu_k + \sigma_k^2$. For an arbitrary parameter,

$$\begin{aligned}
\frac{\partial \ell}{\partial \theta_i} &= \frac{\partial}{\partial \theta_i} \sum_k x_k \log x_k + \mu'_k - x_k \log (\mu'_k) \\
&= \sum_k \frac{\partial \mu'_k}{\partial \theta_i} \left(\frac{\mu'_k - x_k}{\mu'_k} \right)
\end{aligned}$$

$$I_{ij}(\theta) = \mathbb{E}_\theta \left(\sum_k \frac{\partial \mu'_k}{\partial \theta_i} \frac{\partial \mu'_k}{\partial \theta_j} \left(\frac{\mu'_k - x_k}{\mu'_k} \right)^2 \right) = \sum_k \frac{1}{\mu'_k} \frac{\partial \mu'_k}{\partial \theta_i} \frac{\partial \mu'_k}{\partial \theta_j}$$

4.4 Dense localization with convolutional neural networks

We employ a localization CNN architecture based on DeepSTORM which consists of three main modules. A complete mathematical description of the architecture is given in the original paper (Nehme 2020). The first module consists of successive dilated convolutions, followed by an upsampling module to increase the lateral resolution by a factor of 4. The third and last module adds additional convolutional blocks to refine localization estimates. This architecture can also be used for three-dimensional localization and thus the final output has n_z channels. The final output is followed by an element-wise HardTanh (Maas 2013). A post-processing function F_{PP} uses a user-defined threshold to produce a matrix of coordinates. We find the performance of this architecture on simulated images surpasses MLE, and approaches the Cramer-Rao lower bound at high signal levels, retaining a RMSE near 20nm for $K(\lambda/2\text{NA}) \leq 5$, at high signal levels (Figure 3).

4.5 Hidden Markov Model for counting fluorescent emitters

Consider a Poisson hidden Markov model with an unknown state space dimension. Let s_n represent the hidden state at time n , and w_n denote the observed state. The hidden state distribution is parameterized by ϕ , transition matrices by Π , and the initial state by ρ . We

explore various dimensionalities, trying different initial states ρ_i for $i = 1, 2, \dots, 10$. The log likelihood of the observed sequence of states is computed for each dimensionality. The model is implemented using the ‘hmmlearn’ library in Python, utilizing the expectation-maximization algorithm for parameter estimation.

Forward-Backward Algorithm:

The forward algorithm computes the probability of observing a sequence up to time t and being in state s_t :

$$\alpha_t(s) = P(w_1, w_2, \dots, w_t, s_t = s | \phi, \Pi, \rho) = \sum_{s_{t-1}} \alpha_{t-1}(s_{t-1}) \cdot \Pi_{s_{t-1}, s} \cdot P(w_t | \phi_s)$$

The backward algorithm computes the probability of observing the sequence from time $t + 1$ to the end, given being in state s_t :

$$\beta_t(s) = P(w_{t+1}, w_{t+2}, \dots, w_T | s_t = s, \phi, \Pi) = \sum_{s_{t+1}} \beta_{t+1}(s_{t+1}) \cdot \Pi_{s, s_{t+1}} \cdot P(w_{t+1} | \phi_{s_{t+1}})$$

The probability of the observed sequence is given by the product of forward probabilities at the last time step:

$$P(w | \phi, \Pi, \rho) = \sum_{s_T} \alpha_T(s_T)$$

Baum-Welch (EM) Algorithm:

In the E-step, compute the expected number of transitions and emissions:

$$\gamma_t(s) = P(s_t = s | w, \phi, \Pi, \rho) = \frac{\alpha_t(s) \cdot \beta_t(s)}{P(w | \phi, \Pi, \rho)}$$

$$\xi_t(s, s') = P(s_t = s, s_{t+1} = s' | w, \phi, \Pi, \rho) = \frac{\alpha_t(s) \cdot \Pi_{s,s'} \cdot P(w_{t+1} | \phi_{s'}) \cdot \beta_{t+1}(s')}{P(w | \phi, \Pi, \rho)}$$

In the M-step, update the parameters:

$$\rho_s = \frac{\gamma_1(s)}{\sum_{s'} \gamma_1(s')}$$

$$\Pi_{s,s'} = \frac{\sum_{t=1}^{T-1} \xi_t(s, s')}{\sum_{t=1}^{T-1} \gamma_t(s)}$$

$$\phi_s = \frac{\sum_{t=1}^T \gamma_t(s) \cdot w_t}{\sum_{t=1}^T \gamma_t(s)}$$

4.6 Computation of Besag's L-function

Besag's L-function $L(r)$ is a transformation of Ripley's K-function $K(r)$. The estimates of $K(r)$ are of the form

$$K(r) = \frac{a}{n(n-1)} \sum_{ij} I(d_{ij} \leq r)$$

where a is the area of the window, n is the number of data points and the sum is taken over all pairs of points. $I(d_{ij} \leq r)$ is the indicator function which equals 1 if the distance is less than or equal to r . The L-function is then $L(r) = \sqrt{\frac{K(r)}{\pi}}$. For a stationary Poisson process $L(r) = r$, making a $L(r) - r$ a suitable choice for the degree of clustering.

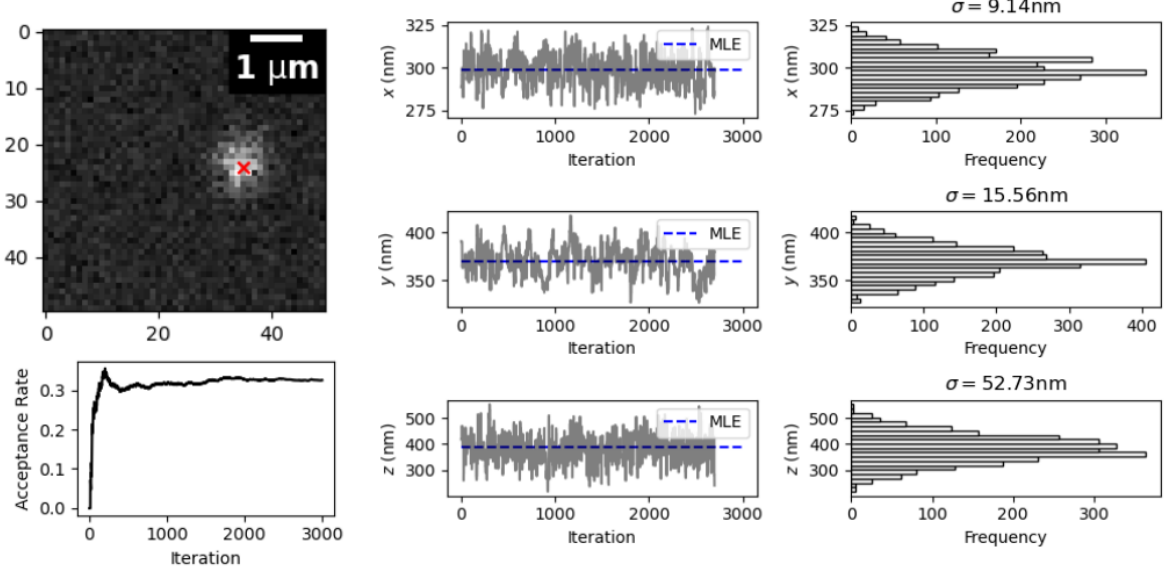


Figure 6: Computing epistemic uncertainties with Metropolis-Hastings. (top left) Simulated point spread function for $N_0 = 10^3$ photons with a red x at x_{MLE} and y_{MLE} (bottom left) Acceptance rate of Markov chain (middle) Markov chains sampling from the posterior distribution on molecule coordinates in 3D, with the maximum likelihood estimation in dashed blue (right) Estimated posterior marginals on the localization parameters with their respective uncertainties

4.7 Fourier Ring Correlation

Following (Nieuwenhuizen 2013), a pair of subsets is drawn from the full list of localizations, and isotropic Gaussian kernel density estimation is performed. The Fourier Ring Correlation is calculated as a function of the ring radius q for two images f_1 and f_2

$$\text{FRC}(q) = \frac{\sum_{\vec{q} \in \text{circle}} \tilde{f}_1(\vec{q}) \tilde{f}_2(\vec{q})^*}{\sqrt{\sum_{\vec{q} \in \text{circle}} |f_1(\vec{q})|^2} \sqrt{\sum_{\vec{q} \in \text{circle}} |f_2(\vec{q})|^2}}$$

where, for example, \tilde{f}_1 is the discrete Fourier transform of f_1 .

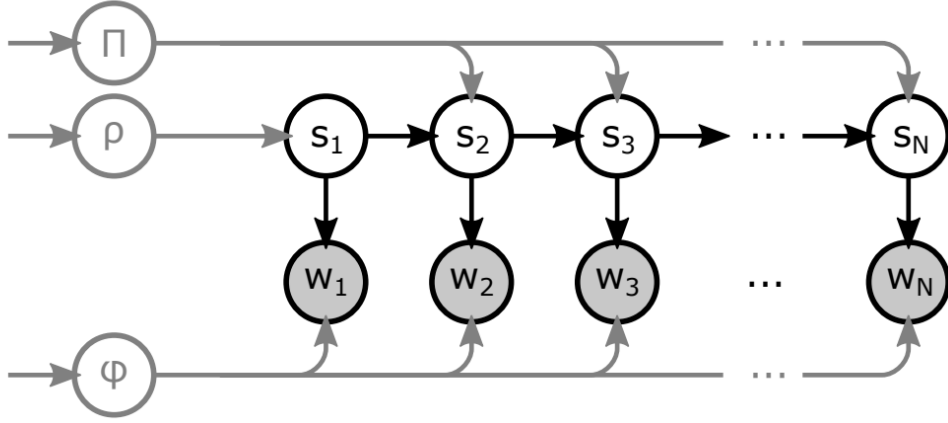


Figure 7: Graphical representation of Hidden Markov Model (HMM) for counting QDs See main text for full description

5 Supplemental Information

5.1 Noise model for CMOS cameras used for MLE

CMOS cameras have noise sources intrinsic to their operation, such as shot noise and read-out noise. The former phenomenon can describe a superposition of processes; namely, the fluctuations of the number of photons due to the quantum nature of light, and the random conversion of photons into photoelectrons within the semiconductor material with a quantum efficiency below unity. Here we will often refer to the photon count N_0 , which has a determined value, rather than being described by statistically. The *measured* photon count, however, is well-described by a Poisson process (Schottky 1918). A shot-noise limited image with N pixels is then described as a family of Poisson variables, with units of photoelectrons

$$\vec{S} = [\text{Poisson}(\mu_1), \text{Poisson}(\mu_2), \dots, \text{Poisson}(\mu_N)] \quad (7)$$

CMOS sensors also suffer from other noise sources, such as readout noise or dark current, resulting in a nonzero signal even in the absence of incident light. Dark current is

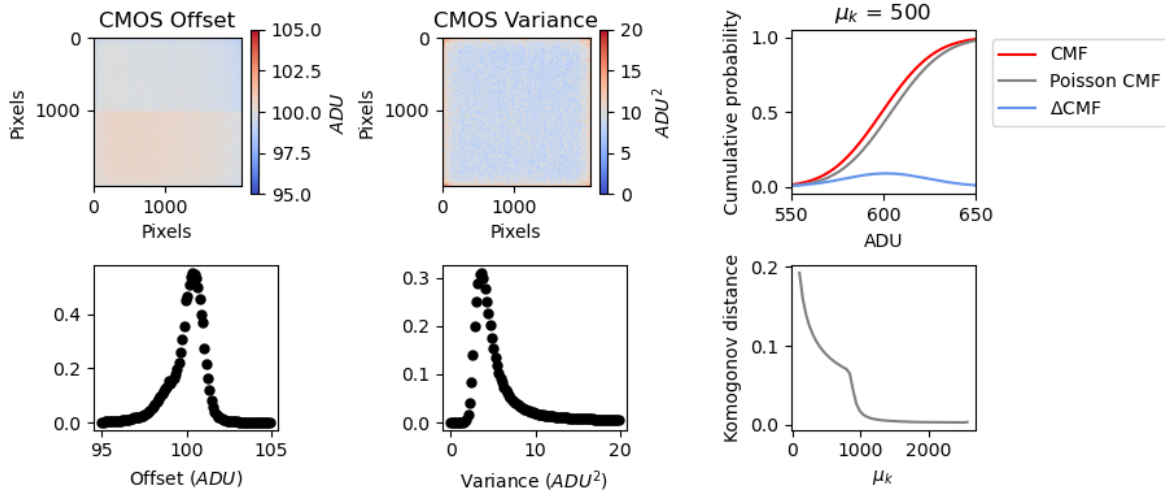


Figure 8: Noise model for CMOS cameras used for MLE. (A) Offset for zero incident photons (B) Variance for zero incident photons (C) Cumulative mass function for the convolution distribution and its Poisson approximation for rate parameter $\mu_k = 500$ counts (D) Komogonov distance measured as a function of rate parameter μ_k

due to statistical fluctuations in the photoelectron count within a semiconductor material in thermal equilibrium. Fortunately, these additional noise sources are governed by the central limit theorem, and can be efficiently summarized as the component of the noise which exhibits a Gaussian distribution. Readout noise has been often neglected in localization algorithms because its presence in EMCCD cameras is small enough that it can be ignored within the tolerances of the localization precision. In the case of high speed CMOS cameras, however, the readout noise of each pixel is significantly higher and, in addition, every pixel has its own noise and gain characteristic sometimes with dramatic pixel-to-pixel variations (Huang 2013). Therefore, accurate localization and simulation necessitates models which incorporate detailed sensor properties.

5.2 Integrated isotropic Gaussian point spread functions

For the sake of simplicity, it is common to describe the point spread function (PSF) as a two-dimensional isotropic Gaussian (Zhang 2007). This is an approximation to the more

rigorous diffraction models given by Richards and Wolf (1959) or Gibson and Lanni (1989).

$$G(x, y) = \frac{1}{2\pi\sigma^2} e^{-\frac{(x-x_0)^2 + (y-y_0)^2}{2\sigma^2}}$$

The characteristic width σ of the PSF typically depends on the numerical aperture of the objective lens. The image of a fluorescent molecule captured by the objective lens, can be thought of as two-dimensional histogram of photon arrivals and a discretized form of the classical intensity profile $G(x, y)$. The value at a pixel approaches an integral of this density over the pixel:

$$\mu_k = i_0 \lambda_k = i_0 \int_{\text{pixel}} G(x, y) dx dy \quad (8)$$

where $i_0 = g_k \eta N_0 \Delta$. The parameter η is the quantum efficiency and Δ is the exposure time. N_0 represents the number of photons emitted per unit time. The above integral can be expressed in terms of error functions, and the full calculation can be found in (Smith 2010).

6 References

- [1] Schermelleh, L. et al. Super-resolution microscopy demystified. *Nature Cell Biology* vol. 21 72–84 (2019).
- [2] Speiser, A. et al. Deep learning enables fast and dense single-molecule localization with high accuracy. *Nat Methods* 18, 1082–1090 (2021).
- [3] Dertinger, T., Colyer, R., Iyer, G., Weiss, S. Enderlein, J. Fast, background-free, 3D super-resolution optical fluctuation imaging (SOFI). *PNAS*
- [4] Richards, B. Wolf, E. Electromagnetic Diffraction in Optical Systems. II. Structure of the Image Field in an Aplanatic System. Source: *Proceedings of the Royal Society of London. Series A, Mathematical and Physical Sciences* vol. 253 (1959).

- [5] Ouyang, W., Aristov, A., Lelek, M., Hao, X. Zimmer, C. Deep learning massively accelerates super-resolution localization microscopy. *Nat Biotechnol* 36, 460–468 (2018).
- [6] Chao, J., Sally Ward, E. Ober, R. J. Fisher information theory for parameter estimation in single molecule microscopy: tutorial. *Journal of the Optical Society of America A* 33, B36 (2016).
- [7] Nehme, E. et al. DeepSTORM3D: dense 3D localization microscopy and PSF design by deep learning. *Nat Methods* 17, 734–740 (2020).
- [8] Nieuwenhuizen, R et al. Measuring image resolution in optical nanoscopy. *Nature Methods* 10. 557-562 (2013).
- [9] Tokunaga, M., Imamoto, N. Sakata-Sogawa, K. Highly inclined thin illumination enables clear single-molecule imaging in cells. *Nat Methods* 5, (2007).
- [10] Kalisvaart, D. et al. Precision in iterative modulation enhanced single-molecule localization microscopy. *Biophys J* 121, 2279–2289 (2022).
- [11] Zhang, B., Zerubia, J. Olivo-Marin, J.-C. Gaussian approximations of fluorescence microscope point-spread function models. (2007).
- [12] Smith, C. S., Joseph, N., Rieger, B. Lidke, K. A. Fast, single-molecule localization that achieves theoretically minimum uncertainty. *Nat Methods* 7, 373–375 (2010).
- [13] Sabari, B. R. et al. Coactivator condensation at super-enhancers links phase separation and gene control. *Science* (1979) 361, (2018).
- [14] Linde, S. Van De et al. Direct stochastic optical reconstruction microscopy with standard fluorescent probes. *Nat Protoc* 6, 991–1009 (2011).
- [15] Huang, F. et al. Video-rate nanoscopy using sCMOS camera-specific single-molecule localization algorithms. *Nat Methods* 10, 653–658 (2013).
- [16] Hnisz, D., Shrinivas, K., Young, R. A., Chakraborty, A. K. Sharp, P. A. A Phase Separation Model for Transcriptional Control. *Cell* vol. 169 13–23 (2017).
- [17] Grimm, J. B. et al. A general method to improve fluorophores for live-cell and single-molecule microscopy. *Nat Methods* 12, 244–250 (2015).

- [18] Nozaki, T. et al. Dynamic Organization of Chromatin Domains Revealed by Super-Resolution Live-Cell Imaging. *Mol Cell* 67, 282-293.e7 (2017).
- [19] Xu, J. et al. Super-Resolution Imaging of Higher-Order Chromatin Structures at Different Epigenomic States in Single Mammalian Cells. *Cell Rep* 24, 873–882 (2018).
- [20] Boettiger, A. N. et al. Super-resolution imaging reveals distinct chromatin folding for different epigenetic states. *Nature* 529, 418–422 (2016).
- [21] Nozaki, T. et al. Dynamic Organization of Chromatin Domains Revealed by Super-Resolution Live-Cell Imaging. *Mol Cell* 67, 282-293.e7 (2017). [3] Barth, R., Bystricky, K. Shaban, H. A. Coupling chromatin structure and dynamics by live super-resolution imaging. *Sci. Adv* vol. 6 (2020).
- [22] Devaiah, B. N. et al. BRD4 is a histone acetyltransferase that evicts nucleosomes from chromatin. *Nat Struct Mol Biol* 23, 540–548 (2016).
- [23] Filippakopoulos, P. et al. Selective inhibition of BET bromodomains. *Nature* 468, 1067–1073 (2010).
- [24] Grimm, J. B. et al. A General Method to Improve Fluorophores Using Deuterated Auxochromes. *JACS Au* 1, 690–696 (2021).
- [25] Itoh, Y. et al. 1,6-hexanediol rapidly immobilizes and condenses chromatin in living human cells. *Life Sci Alliance* 4, (2021).
- [26] Han, X. et al. Roles of the BRD4 short isoform in phase separation and active gene transcription. *Nat Struct Mol Biol* 27, 333–341 (2020).
- [27] Los, G. V. et al. HaloTag: A novel protein labeling technology for cell imaging and protein analysis. *ACS Chem Biol* 3, 373–382 (2008).
- [28] Bannister, A. J. Kouzarides, T. Regulation of chromatin by histone modifications. *Cell Research* vol. 21 381–395 (2011).
- [29] Ricci, M. A., Manzo, C., García-Parajo, M. F., Lakadamyali, M. Cosma, M. P. Chromatin fibers are formed by heterogeneous groups of nucleosomes in vivo. *Cell* 160, 1145–1158

(2015).